Viscous-flow approach to *in-situ* infiltration and to *in-vitro* K_{sat}-determination

Peter F. Germann*) and Michel Karlen

Geographisches Institut

Universität Bern (Switzerland)

*) Corresponding author: pf.germann@bluewin.ch

Vadose Zone J.
doi:10.2136/vzj2015.05.0065
Received 1 Apr. 2015.
Accepted 13 Oct. 2015.

Vol. 15, Iss. 2, 2016

Abstract

Infiltration is dominantly gravity driven. Thus, the viscous-flow approach to infiltration and drainage is based on laminar film flow. Its hydro-mechanical base is the equilibrium between the viscous and the gravity force. This leads to a constant flow velocity during a period lasting 3/2 times the duration of a constant input rate, q_S. The key parameters of the approach are the film thickness F and the specific contact area L of the film per unit soil volume. Calibration of the approach requires at some depth any pair of the three time functions volume flux density, mobile water content, and velocity of the wetting front. Sprinkler irrigation produces *in-situ* time series of volumetric water contents, $\theta(z,t)$, as determined with TDR-probes. The wetting front velocity v and the time series of the mobile water content, $w(z,t)$ are deduced from $\theta(z,t)$. *In-vitro* steady flow in a core of saturated soil provides volume flux density, $q(z,t)$, and flow velocity, v, as determined from heat front velocity. The viscous-flow approach is introduced in details, and the F- and L- parameters of the *in-situ* and the *in-vitro* experiments are compared. The macropore-flow restriction states that, for a particular permeable medium, the specific contact area L be independent from q_s i.e., $\mathrm{d}L/\mathrm{d}q_S = 0$. If true, than the relationship of $q_S \propto v^{3/2}$ could scale a wide range of input rates $0 \leq q_S \leq K_{sat}$ into a particular permeable medium, and kinematic-wave theory would become a versatile tool to deal with non-equilibrium flow. The viscous-flow approach is based on hydro-mechanical principles similar to Darcy's (1856) law, but currently it is not suited to deduce flow properties from specified individual spatial structures of permeable media.

Key words

Capillary flow, saturated flow, viscous flow, Reynolds number, temperature tracer, kinematic-wave theory.

Introduction

Infiltration is the transgression of liquid water from above ground to below ground, and subsequent seepage, while gravity primarily drives flow. Approaches to infiltration are commonly based on Richards' (1931) capillary flow i.e., the Richards equation. The hydraulic property functions $\psi(\theta)$ and $K(\theta)$ are the core of the approach, where ψ (Pa), θ (m^3 m^{-3}), and K (m s^{-1}) are capillary potential, volumetric water content, and hydraulic conductivity, respectively. While gravity provides one part of the flow-driving gradient, $\psi(\theta)$ is the base for its capillary part. In the sense of Darcy (1856), K_{sat} m s^{-1} summarizes the inverse of resistance to flow in saturated porous media, regardless of the actual shares of the flow-participating water and the paths it follows. However, sequential flow is a mandatory condition for relating K with θ in the case of unsaturated flow. Accordingly, wider voids have to empty before smaller ones do during drainage, while the smaller ones have to fill before the larger ones do during imbibition.

Non-equilibrium flow in the sense of the Richards equation, for instance according to Jarvis (2007), embraces all the non-sequential flows which are summarized here as preferential flow (Germann, 2014). Actually, the term *non-equilibrium* with respect to Richards' capillary flow implicitly admits an incomplete hydro-mechanical analysis of the flow process in view of the mass-, momentum-, and energy-balance.

Dual-permeability approaches are frequently applied to mend the shortcomings of non-equilibrium flow, where a permeable medium is divided into a fast- and a slow-flow domain. Among other approaches, the Richards (1931) equation is frequently applied to both domains after due calibration, and hydraulic interactions are allowed between the two domains. Coppola et al. (2012), for example, presented a dual-permeability model for preferentail infiltration into soils with fractures originating from shrinking. The fractures constitute the fast-flow domain and the matrix the slow-flow counterpart. From closer ocular inspection of the photograph in their Fig. 3 follow approximate widths of about F=5 x 10^{-3} m and of specific densities of the fractures of L=1 m m^{-2}. The water content in the fracture system during saturated infiltration becomes $\theta_{fr} = L \times F = 5 \times 10^{-3}$ m^2 m^{-2}. Inserting F into Poisson's law results in ψ_{fr} = - 30 Pa (the subscript *fr* refers to the fracture domain). Inserting F into Poiseuille's law and assuming gravity to be the only driving force leads to the approximate volume flux density of $q_{fr} = 5 \times 10^{-2}$ m s^{-1}. The wetting front velocity is $v_{fr} = q_{fr} / \theta_{fr} = 10$ m s^{-1}, and the corresponding Reynolds number amounts about to $Re = (F \times v_{fr} \times \rho)/\mu = 5 \times 10^4$, where $\mu = 10^{-3}$ Pa s is the dynamic viscosity of water. The results of the hydro-mechanical analysis of fracture flow in Coppola et al. (2012) are disturbingly counter-intuitive. In particular, the enormous Reynolds number forecloses the application of any Darcy- and Richards-type flow which require $Re \approx 1$. Soils themselves demonstrate that fully saturated macropore flows must be rare events. Turbulent flow, as demonstrated with Coppola et al. (2012), persisting over considerable time would lead to severe internal erosion and eventually to the collapse of soil profiles.

Alberti and Cey (2011), simulating infiltration from tension infiltrometers with an approach similar to the one of Coppola et al. (2012), circumvented the hydro-mechanical contradiction by numerically reducing to 3 x 10^{-4} m the observed macropore diameters of 5 x 10^{-3} m. The experience led Alberti and Cey (2011) to challenge the Richards equation which " … *may be an invalid representation for macropore flow processes*."

Adherence to Richards-type flow also has to adhere to sequential flow in each of the two flow domains. Whereas the step-wise determination of $\psi(\theta)$ and $K(\theta)$ in mono-porous systems is straight forward under the experimental constraints set by the Richards equation, the corresponding experimental procedure for dual-porosity media is much more involved, as the numerous parameters of flow models indicate. Dual-porosity, dual-permeability, and similar approaches are saddled with providing clear criteria for separating the two domains of pores or flows, preferably with hydromechanically sound arguments. Macropores of various sorts are frequently used to characterize the fast-flow pores but mostly with subjective definitions. However, proper delineation of the two domains is mandatory. The example of Alberti and Cey (2011), who numerically reduced the diameter of macropores by a factor of about 15 in order to match observations of flow with model performance, illustrates the hydro-mechanical sensitivity of the delineation procedure. According to Poiseuille-flow, the reduction of the macropore diameter also reduced the volume flux in each macropore by the fourth power i.e., by $15^4 \approx 50000$, and *Re* dropped from more than 10^4 to 2 i.e., from fully turbulent to laminar flow. The uncertainty in the delineation decision on the one hand and the hydro-mechanical sensitivity resulting from the uncertainty on the other hand call for fundamental hydro-mechanical considerations of approaching preferential flow rather than focusing on sophisticated optimization procedures with long- existing and well entrenched numerical codes that are based on capillary flow and that were not primarily designed for dealing with gravity-dominated infiltration.

Viscous flow provides for an alternative to sequential capillary flow. During infiltration, flow in non-saturated porous media is considered as purely gravity-driven. Momentum diffusion due to viscosity opposes the driving force to such an extent that constant flow velocities occur over a period lasting 3/2 times the duration of water application to the soil surface. Germann and al Hagrey (2008), among others, provide an example of constant wetting front velocity over a period lasting more than 16 h and stretching over a depth range of 2 m. Later on the velocity of the wetting front greatly reduces. Capillarity abstracts water from the viscous-flow domain to the remaining porous medium, while capillarity and viscosity coexist (Germann, 2014).

The manuscript presents the viscous-flow relationships and applies them to the data of Karlen (2008) which were derived

a) from *in-situ* sprinkler-infiltration experiments into a soil with a high antecedent water content, and

b) from *in-vitro* core flows of saturated soil used to determine K_{sat}.

The core samples were taken from the profile of the *in-situ* infiltration experiments. The procedure permits direct comparisons of *in-situ* infiltration at high degree of saturation with *in-vitro* determination of K_{sat}. Moreover, the macropore-flow restriction will be introduced. If the restriction is true, than kinematic-wave theory applies to a wide variation of input rates, and the easy *in-vitro* determination of the two flow parameters film thickness F and specific contact length L will be applicable to a broad range of infiltration rates.

Theory

Input to the soil surface is a rectangular water pulse $P(q_S,T_B,T_E)$ which is characterized by the volume flux density q_S, and the times T_B and T_E of its beginning and ending. The subscript S refers to the surface. A water content wave *WCW* starts moving into the soil when P hits the soil surface at T_B. Figure 1 depicts the major part of a *WCW* which summarizes the spatio-temporal function of the mobile water content, $w(z,t)$ m^3 m^{-3}, under the auspice of viscous flow.

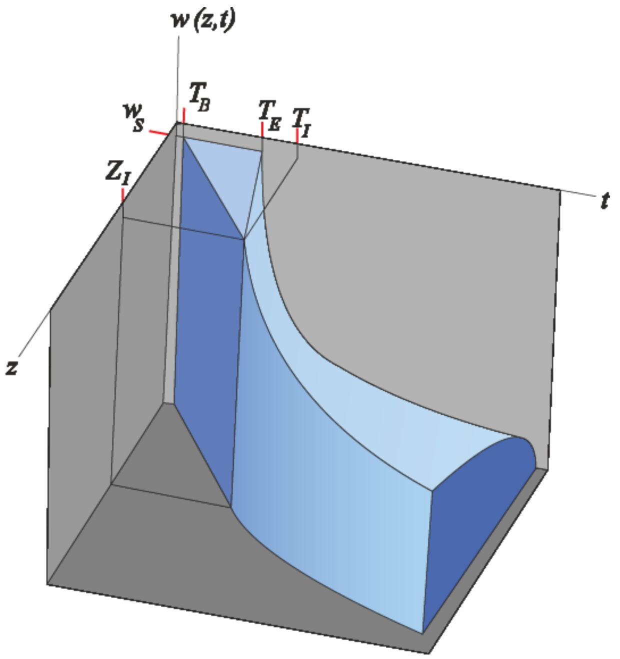

Figure 1: Water Content Wave *WCW, w(z,t)*, as response to a rectangular input pulse $P(qs,T_B,T_E)$. w_S represents the mobile water content which forms spontaneously in a particular permeable medium as response to P; the times T_B and T_E are the beginning and ending of P; Z_I and T_I are depth and time of the wetting front intercepting the draining front.

Any time-variable water input to the soil surface is approachable with a series of such pulses, and superposition leads to a composite *WCW*. However, this contribution deals only with the propagation of a single pulse, whose evolution is now considered under the following six prerequisites:

(i) Only gravity drives flow, and no additional pressure is acting on the water. (Later on, the restriction will be relaxed to include pressure gradients as part of the flow-driving force).

(ii) Mobile water *w* moves as film. One side of it glides along the stationary parts of the porous medium generally consisting of solid, sessile water and air. Here the non-slip condition prevails. The other side of the film is exposed either to the air or to the water surface of the opposite and parallel water film in case of saturated flow paths.

(iii) Viscous flow prevails along the paths.

(iv) There is no viscous flow in the permeable medium prior to the arrival of the first pulse at the surface.

(v) The total volume of water applied to the soil surface remains preserved within the *WCW* i.e., there are neither gains nor losses to and from the *WCW*. (Later on, this restriction will be relaxed to account for water abstraction from the *WCW* due to capillarity.)

(vi) Low Reynolds number $Re \approx 1$.

The six prerequisites do neither require homogeneous permeable media nor homogeneous antecedent water contents.

The following provides the hydro-dynamics of viscous flow leading to the *WCW*. Consider Fig. 2, where *F, f*, and d*f*, all in m, represent the film thickness, the film thickness variable ($0 \leq f \leq F$), and the thickness of a lamina; L m^{-1} is the specific contact length per unit of the horizontal cross-sectional area A m^2 between the mobile water film and the static part of the system; $z_W(t)$ m is the temporal position of the wetting shock front of the *WCW*.

Newton (1729) postulated the hypothesis of shear as *"The resistance, arising from the want of lubricity in the parts of a fluid, is,* caeteris paribus*, proportional to the velocity with which the parts of the fluid are separated from each other. "* Newton's (1729) hypothesis leads to the shear force at *f* as

$$\varphi(f) = -\eta \cdot \rho \cdot \left. \frac{\mathrm{d}\,v(f)}{\mathrm{d}\,f} \right|_f \qquad [1]$$

N m^{-2}, where ρ kg m^{-3} is the density of water and $v(f)$ m s^{-1} represents the velocity of the lamina at *f*, d$v(f)$/d*f* is the velocity gradient at *f*, while dimensional analysis yields m^2 s^{-1} for η. It scales the diffusion of momentum, ρ x $v(f)$, at f with η acting as the diffusion coefficient which Maxwell(1866) called the kinematic viscosity (of water in our case). Equation [1] holds for incompressible liquids.

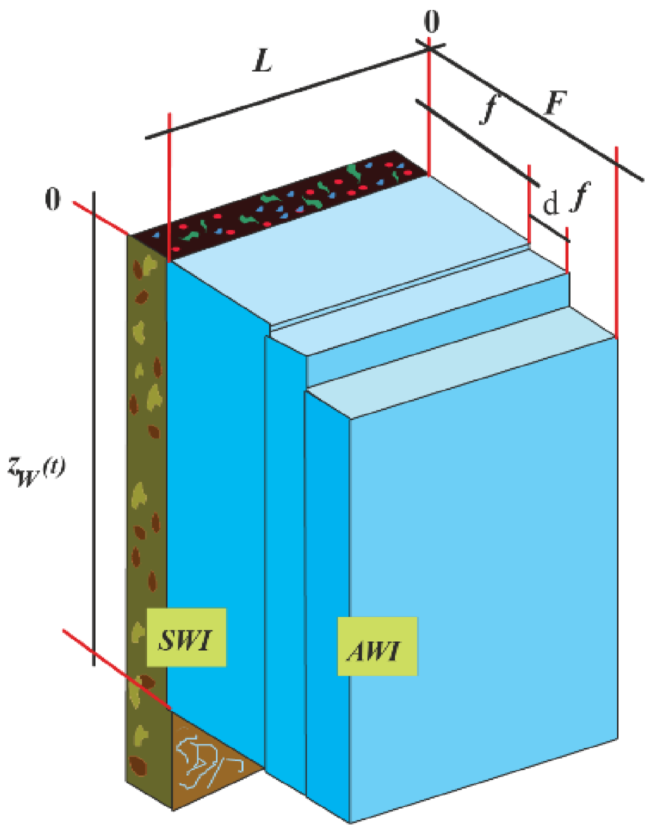

Figure 2: Schematic representation of film flow. F, f, and d f represent the film thickness, the film thickness variable ($0 \leq f \leq F$), and the thickness of a lamina, $z_W(t)$ is the time-dependent depth of the wetting front, L is the contact length per unit cross-section of the horizontal area A (L is also the vertical surface area per unit volume of the permeable medium onto which momentum diffuses),while *SWI* and *AWI* are the solid-water and the air-water interfaces of the film.

The weight of the moving water film ρ x g x L x $z_W(t)$ x (F-f) N m^{-2}, per unit volume of soil, A x $z_W(t)$ is balanced by $\varphi(f)$ acting at f within the vertical specific area per unit volume of soil, L x A x $z_W(t)$/ [A x $z_W(t)$]. Note that L also represents the specific vertical area per unit volume of the permeable medium onto which momentum diffuses. Thus, $\varphi(f)$ at f balances the weight of the film from f to F:

$$\eta \cdot \rho \cdot L \cdot z_W(t) \cdot \left.\frac{dv}{df}\right|_f = \rho \cdot g \cdot L \cdot z_W(t) \cdot (F - f) \qquad [2]$$

Pa, where g m s^{-2} is acceleration due to gravity. Integrating Eq. [2] from the solid-water interface, *SWI*, where $v(0) = 0$ (non-slip condition), to f yields the parabolic velocity profile of

$$v(f)=\frac{g}{\eta}\cdot(F\cdot f-\frac{f^2}{2}) \qquad [3]$$

m s^{-1}. The differential volume flux density at *f* is

$$\mathrm{d}q\big|_f = L\cdot v(f)\cdot \mathrm{d}f \qquad [4]$$

m s^{-1}. Its integration from the *SWI* at *f* = 0 to the air-water interface, *AWI,* at *f* = *F* produces the volume flux density of the film as

$$q(F,L)=\frac{g}{3\cdot\eta}\cdot L\cdot F^3 \qquad [5]$$

m s^{-1}, while the mobile water content amounts to

$$w(F,L)=F\cdot L \qquad [6]$$

m^{3}m^{-3}. Note the distinction between the mobile water content *w* according to Fig. 2 and the total water content θ m^{3}m^{-3} of the permeable medium. The velocity of the wetting shock front follows from the volume balance amounting to

$$v(F)=\frac{q(F,L)}{w(F,L)}=\frac{g}{3\cdot\eta}\cdot F^2 \qquad [7]$$

m s^{-1}, where *F* is the only variable impacting *v(F).* Moreover,

$$z_W(t)=v(F)\cdot(t-T_B) \qquad [8]$$

The convenient relationships allow for a concept of flow in permeable media without *a-priori* considerations of the size and geometry of flow paths. The combination of Eq. [5] with Eq. [6] yields the volume flux density as function of the mobile water content

$$q(w)=\frac{g}{3\cdot\eta\cdot L^2}\cdot w^3 \qquad [9]$$

The celerity *c* m s^{-1} is the velocity of any change d*q*/d*w* in the *WCW*. Thus, combination of Eq. [6] with Eq. [9] leads to the celerity of the *WCW* as

$$c(F)=\frac{\mathrm{d}q}{\mathrm{d}w}=\frac{g}{\eta}\cdot F^2=3\cdot v(F) \qquad [10]$$

The total Volume of the *WCW* amounts to

$$Q_S=q_S\cdot(T_E-T_B) \qquad [11]$$

m. Lin and Wan (1986) limited viscous flow in permeable media to Reynolds numbers *Re* ≤ 3. Thus,

$$Re=\frac{F\cdot v}{\eta}=\frac{F^3\cdot g}{3\cdot\eta^2}=\left(\frac{3\cdot v^3}{g\cdot\eta}\right)^{1/2}\leq 3 \qquad [12]$$

which leads to the approximate maxima of F_{max} ≈ 100 µm and v_{max} ≈ 30 mm s^{-1}.

The cessation of input to the surface at [$t = T_E$] cuts off flow, and the thickness of the water film at [$z = 0$] instantaneously collapses from F to 0 while Q_S remains. The sudden cut-off at T_E releases the upper ends of all the laminae at [$z = 0$], Fig. 2, while the laminae themselves continue to glide one over the other. The upper end of the lamina at F represents the draining front that moves the fastest with the wave velocity $c(F)$, and whose position is

$$z_D(t) = c \cdot (t - T_E) \qquad [13]$$

Under consideration of Eqs. [8, 13], the wetting front $z_W(t)$ eventually intercepts the draining front $z_D(t)$ at depth

$$Z_I = v \cdot (t - T_B) = c \cdot (t - T_E) = \frac{c}{2} \cdot (T_E - T_B) \qquad [14]$$

and at time

$$T_I = T_B + \frac{Z_I}{v} = T_E + \frac{Z_I}{c} = \frac{1}{2} \cdot (3 \cdot T_E - T_B) \qquad [15]$$

T_I depends only on the duration of the pulse [T_E-T_B].

The following leads to the shape of the trailing wave, $w(z,t)$, during [$T_E \leq t \leq T_I$]. The water film starts to physically disintegrate beyond the line from $w(0, T_E)$ to $w(Z_I, T_I)$, Fig. 1. This is reflected mathematically in the reversing of integration which describes the formation of the collapsing trailing wave. A lamina at the arbitrary distance f carries the volume flux density dq and the water content L x df . From volume balance requirements follows the velocity of its upper end as

$$c_{up}(f) = \left.\frac{dq}{df}\right|_f \cdot \frac{1}{L} = \frac{z_{up}(f)}{t(z_{up}) - T_E}, \qquad [16]$$

where $z_{up}(f)$ m is the position of the upper end of the lamina at f at time $t(z_{up})$. Upon inserting the first derivative from the equivalent of Eq. [5],

$$\frac{\mathrm{d}q}{\mathrm{d}f} = \frac{g}{\eta} \cdot L \cdot f^2, \qquad [17]$$

into Eq. [10] we get

$$c_{up}(f) = \frac{z_{up}(f)}{(t - T_E)} = \frac{g}{\eta} \cdot f^2. \qquad [18]$$

Rearranging the central and right-hand parts of Eq. [18] and solving for f leads to the temporal position of the film thickness. Its multiplication with L provides the spatio-temporal distribution of the mobile water content of the *WCW* during [$T_E \leq t \leq T_I$] as

$$w(z,t) = L \cdot \left(\frac{\eta}{g}\right)^{1/2} z^{1/2} (t - T_E)^{-1/2} \qquad [19]$$

After $t > T_I$ and beyond $z > Z_I$ the *WCW* loses the plateau and becomes crested, the draining front disappears, and $v(z,t)$ decreases with time and depth. The shape of the profile of mobile water according to Eq. [19] remains over the entire depth range extending from the surface to the wetting front, $0 \le z \le z_W(t)$, in particular also during $t \ge T_I$. The depth integral of $w(z,t)$ at any time $t \ge T_I$, according to Eqs. [11, 19] is:

$$Q_S = \left(\frac{\eta}{g}\right)^{1/2} \cdot L \cdot (t - T_E)^{-1/2} \cdot \int_0^{z_W(t)} z^{1/2}\, dz \qquad [20]$$

Solving Eq. [20] for $z_W(t)$ yields the temporal position of the wetting front as

$$z_W(t) = \left(\frac{3 \cdot Q_S}{2 \cdot L}\right)^{2/3} \cdot \left(\frac{g}{\eta}\right)^{1/3} \cdot (t - T_E)^{1/3}. \qquad [21]$$

The first derivative of Eq. [21] produces the velocity of the wetting front as

$$v(t)\big|_{z_W} = \left(\frac{Q_S}{2 \cdot L}\right)^{2/3} \cdot \left(\frac{g}{3 \cdot \eta}\right)^{1/3} \cdot (t - T_E)^{-2/3}. \qquad [22]$$

Inserting $z_W(t)$ from Eq. [21] into Eq. [19] yields the mobile water content at the wetting front as

$$w(t)\big|_{z_W} = \left(\frac{\eta}{g}\right)^{1/3} \cdot \left(\frac{3 \cdot Q_S}{2}\right)^{1/3} \cdot (t - T_E)^{-1/3} \cdot L^{2/3} \qquad [23]$$

Multiplication of Eq. [22] with Eq. [23] produces the volume flux density at the wetting front as

$$q(t)\big|_{z_W} = \frac{Q_S}{2 \cdot (t - T_E)} \qquad [24]$$

Time series of $w(\zeta,t)$ at the three depth ranges ζ_i ($1 \le i \le 3$), of $0 \le \zeta_1 < Z_I$, $\zeta_2 = Z_I$, and $\zeta_3 \ge Z_I$ are now considered.

(i) $0 \le \zeta_1 < Z_I$: The arrival times of the wetting and draining fronts at ζ_1 are

$$t_W(\zeta_1) = T_B + \frac{3 \cdot \eta}{g} \cdot F^{-2} \cdot \zeta_1 \qquad [25]$$

$$t_D(\zeta_1) = T_E + \frac{\eta}{g} \cdot F^{-2} \cdot \zeta_1 \qquad [26]$$

while the mobile water content assumes the following values during the respective time intervals:

$$T_B \le t \le t_W(\zeta_1) \qquad w(\zeta_1, t) = 0 \qquad [27]$$

$$t_W(\zeta_1) \le t \le t_D(\zeta_1) \qquad w(\zeta_1, t) = L \cdot F = w_S \qquad [28]$$

$$t \ge t_D(\zeta_1) \qquad w(\zeta_1, t) = L \cdot F \cdot \left(\frac{t_D(\zeta_1) - T_E}{t - T_E}\right)^{1/2} \qquad [29]$$

Equation [29] results from solving Eq. [26] for ζ_1, and substituting with it the depth z in Eq. [19].

(ii) $\zeta_2 = Z_I$: At depth of front interception and after $t \geq T_I$ the mobile water content becomes

$$w(\zeta_2, t) = L \cdot F \cdot \left(\frac{T_E - T_B}{2 \cdot (t - T_E)} \right)^{1/2} \qquad [30]$$

Equation [30] results from replacing $t_D(\zeta_1)$ in Eq. [29] with T_I, Eq. [15].

(iii) $\zeta_3 \geq Z_I$: Solving Eq. [21] for t yields the arrival time of the wetting front at ζ_3 as

$$t_W(\zeta_3) = T_E + \frac{4}{9} \cdot \frac{\eta}{g} \cdot \left(\frac{L}{Q_S} \right)^2 \cdot \zeta_3^{\ 3} \qquad [31]$$

Inserting Eq. [31] into Eq. [19] yields the mobile water content at the crest as

$$w_{crest}(\zeta_3) = \frac{3}{2} \cdot Q_S \cdot \frac{1}{\zeta_3}, \qquad [32]$$

and the mobile water content as a function of time becomes

$$T_B \leq t \leq t_W(\zeta_3) \qquad w(\zeta_3, t) = 0 \qquad [33]$$

$$t \geq t_W(\zeta_3) \qquad w(\zeta_3, t) = \frac{3}{2} \cdot Q_S \cdot \frac{1}{\zeta_3} \cdot \left(\frac{t_W(\zeta_3) - T_E}{t - T_E} \right)^{1/2} \qquad [34]$$

Viscous flow permits the separation of the spatial from the temporal relationships, thus elegantly circumventing the necessity of solving partial differential equations. The exclusive dealing with ordinary differential equations results in a set of comfortably solvable analytical expressions. Figure 3 depicts two time series of $w(\zeta,t)$ in the depth range (i), and one series each in the depth ranges (ii) and (iii).

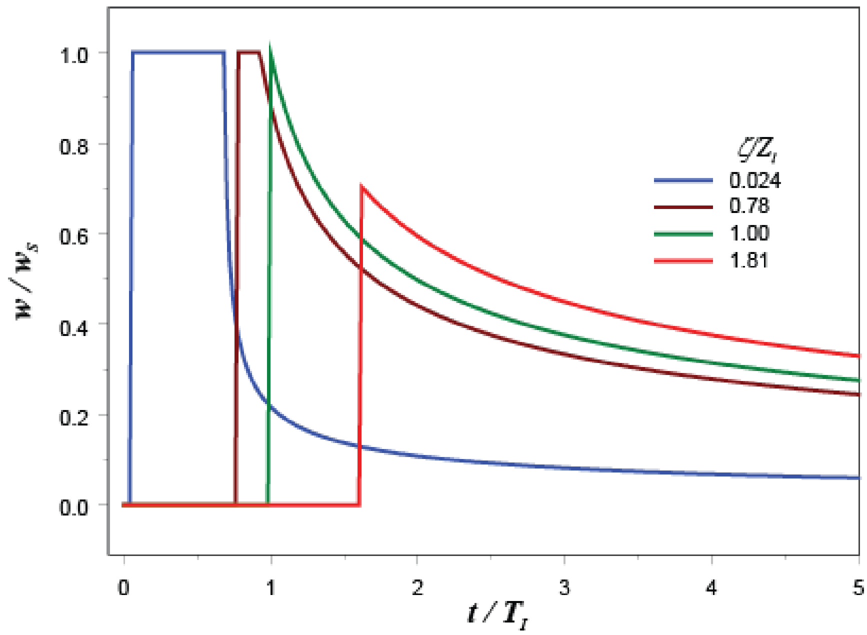

Figure 3: Four standardized *w(ζ,t)*-series according to Eq. [25 to 34].

Volume of viscous flow, $Q(z,t)$ m, at $z < Z_I$ during $t > t_D(z)$ results from piece-wise integrating Eq.[28] from $t_W(z)$ to $t_D(z)$ and Eq. [29] from $t_D(z)$ to t under consideration of Eq. [9], yielding

$$Q(z,t) = F^3 \cdot L \cdot \frac{g}{3 \cdot \eta} \cdot \left(3 \cdot t_D(z) - 2 \cdot T_E - t_W(z) - 2 \cdot \frac{(t_D(z) - T_E)^{3/2}}{(t - T_E)^{1/2}} \right) \qquad [35]$$

The parameters F and L together with $P(q_S,T_B,T_E)$ completely describe a *WCW*. Given $Z_m < Z_I$, where Z_m is the depth in the permeable medium where time series of either $w(Z_m,t)$ or $q(Z_m,t)$ is measured. It is easy to observe the depth-restriction of Z_m in view of Eq. [15] simply by extending T_E accordingly. Because both series, $w(Z_m,t)$ and $q(Z_m,t)$, are reactions on $P(q_S,T_B,T_E)$ that are recorded at the pre-set depth Z_m it follows that

$$v = \frac{Z_m}{t_W(Z_m) - T_B} \qquad [36]$$

where $t_W(Z_m)$ is the time of first significant increase of either w or q at Z_m. The parameters w_{max} and q_{max} represent the amplitudes of the respective time series $w(Z_m,t)$ and $q(Z_m,t)$ as shown in Fig. 3 for $w(\zeta_1,t)$ and Eqs. [25-29]. Experimental determination of F and L relies conclusively on one of the following three combinations:

Combination I if the experiment produces q_{max} and v [or c with $v = c/3$],

$$F = \sqrt{\frac{3 \cdot \eta \cdot v}{g}} \qquad L = q_{max} \cdot \sqrt{\frac{g}{3 \cdot \eta \cdot v^3}} \qquad [37], [38]$$

Combination II if the experiment produces w_{max} and v [or c with $v = c/3$],

$$F = \sqrt{\frac{3 \cdot \eta \cdot v}{g}} \qquad L = w_{max} \cdot \sqrt{\frac{g}{3 \cdot \eta \cdot v}} \qquad \text{[37], [39]}$$

Combination III if the experiment produces w_{max} and q_{max} ,

$$F = \sqrt{\frac{3 \cdot \eta \cdot q_{max}}{g \cdot w_{max}}} \qquad L = \sqrt{\frac{g \cdot w_{max}^{\ 3}}{3 \cdot \eta \cdot q_{max}}} \qquad \text{[40], [41]}$$

Presumed geometry of flow paths

So far film flow was assumed. Germann (2014) compared theoretically free-surface flow, Eq. [1 to 41], with Hagen-Poiseuille flow in cylindrical tubes, and with plane-Poiseuille flow between two parallel walls. He concluded that the variation among the types of flow is less than a factor of 2. The variations among presumed flow-path geometries is thus considered less severe than the uncertainties evolving from generally applying viscous flow.

Co-existence of capillarity and viscosity

Laminar flow requires a low Reynolds-number resulting in $F <\approx 100$ µm, Eq. [12], which is in the range of capillarity. Thus, the coexistence of capillarity and viscosity needs to be addressed. The water's surface tension in an unsaturated permeable medium pulls the solid parts together, the so-called sand-castle effect. However, Flammer et al. (2002) demonstrated that the pulling force remains constant during early times of infiltration despite increasing soil moisture. They measured acoustic velocities across a column of an undisturbed soil. The acoustic velocity depends strongly on the pressure-wave modulus which expresses the rigidity of the medium. Thus, rigidity did not decrease as soil moisture increased. This indicates the co-existence of viscosity and capillarity and it also demonstrates non-equilibrium flow in view of the Richards (1931) equation.

Lazouskaya et al. (2006) tracked with a confocal microscope the movement of µm-particles in rectangular channels which were 0.5 mm wide. Surface tension across the channel provided for a water blanket, while viscous flow prevailed underneath the blanket as the parabolic velocity profiles revealed.

Saturated viscous-flow

Viscous-flow parameters of unsaturated *in-situ* infiltration will be compared with those of saturated flow in core samples used to the *in-vitro* determination of K_{sat}. Thus, three cases of vertical flow need to be considered:

(i) gravity-driven viscous flow in non-saturated porous media:

$$\theta < \varepsilon: \qquad q = \frac{F^3 \cdot L}{3 \cdot \mu} \cdot \rho \cdot g \qquad v = \frac{F^2}{3 \cdot \mu} \cdot \rho \cdot g \qquad [5], [7]$$

where ε m^3 m^{-3} is porosity and the dynamic viscosity is defined as μ = η x ρ.

(ii) gravity-driven viscous flow at saturation:

$$\theta = \varepsilon: \qquad q_{sat} = \frac{F_{sat}{}^3 \cdot L_{sat}}{3 \cdot \mu} \cdot \rho \cdot g = K_{sat} \qquad [42]$$

$$v_{sat} = \frac{F_{sat}{}^2}{3 \cdot \mu} \cdot \rho \cdot g \qquad [43]$$

(iii) viscous flow driven by an external pressure gradient, $(\Delta p/\Delta z) > (\rho\ g)$ kg s^{-2} m^{-2}:

$$\theta = \varepsilon: \qquad q(p) = \frac{F_{sat}{}^3 \cdot L_{sat}}{3 \cdot \mu} \cdot \frac{\Delta p}{\Delta z} = q_{sat} \cdot \frac{\Delta p}{\Delta z \cdot \rho \cdot g} \qquad [44]$$

$$v(p) = \frac{F_{sat}{}^2}{3 \cdot \mu} \cdot \frac{\Delta p}{\Delta z} = v_{sat} \cdot \frac{\Delta p}{\Delta z \cdot \rho \cdot g} \qquad [45]$$

Darcy's law states that $q \propto \Delta p/\Delta z$ i.e., volume flux density is a linear function of the flow-driving pressure gradient with the proportionality factor K_{sat}. In view of the various dimensionalities of $w \propto (L^1, F^1)$, $v \propto (L^0, F^2)$, and $q \propto (L^1, F^3)$, linearity seems only possible if F_{sat} and L_{sat} remain constant and independent from p in the transition from gravity-driven to pressure-driven viscous flow in saturated permeable media i.e., in the transition from Eq. [42] to Eq. [44] and Eq. [43] to Eq. [45]. As a consequence, $w = q/v$ also remains constant. Further, if $\theta = \varepsilon$, $dL_{sat}/dp = 0$ and $dF_{sat}/dp = 0$ then follows that F_{sat} and L_{sat} represent F_{max} and L_{max}, the maxima of a particular porous medium, leading to K_{sat}.

Macropore-flow restriction

Macropore flow is viewed as a special case of viscous flow because, per definition, flow is supposed to follow along the same paths regardless of the boundary and initial conditions. The resulting macropore-flow restriction states that the specific surface area onto which momentum diffuses does not depend on the volume flux density of infiltration, thus

$$\frac{\mathrm{d}L}{\mathrm{d}q_S}=0 \qquad [46]$$

From the combination of Eq. [5] and [7] then follows that

$$v(q_S)=q_S^{\,2/3}\cdot L^{-2/3}\cdot\left(\frac{g}{3\cdot\eta}\right)^{1/3} \qquad [47]$$

The macropore-flow restriction, Eq. [46], implies that *L* is determinable with Eq. [47] from just one pair of v-q_S-values. Consequently, Eqs. [1-24] were then applicable over the entire range of $0 < q_S \leq K_{sat}$ of a particular permeable medium. Moreover, viscous-flow methodology would greatly advance if *L* in [47] could be determined in the laboratory, for instance, through some extension of the K_{sat}-methodology, Eqs. [42-45]. There are indeed indications that the macropore-flow restriction, Eq. [46], and the consequence thereof, Eq. [47], apply. From infiltration experiments using glass beads Shiozawa and Fujimaki (2004) reported ratios of infiltration rates of $q_1/q_2 = 30$ and of the corresponding observed wetting front velocities of $v_1/v_2 = 10$. Scaling under the assumed macropore-flow restriction would lead to $(q_1/q_2)^{2/3} = 30^{2/3} = 9.65$ which is within 3.5 % of the observed value of 10. Likewise, Hincapié and Germann (2009b) demonstrated experimentally that $v \propto q_S^{2/3}$, Eq. [47], applies to infiltrations with a coefficient of determination of $r^2 = 0.95$. They infiltrated input rates of 5, 10, 20, and 40 mm h^{-1} into a column of an undisturbed Mollic Cambisol (FAO-UNESCO, 1994).

Experimental

The investigations aim at the comparison of viscous flow derived from *in-situ* sprinkler experiments with *in-vitro* K_{sat} determined on cores sampled from the same field site. The following strictly separates the field procedures from the laboratory procedures, including the discussions about the methods, because the *in-situ* experiments are based on Combination II, Eqs. [37, 39], while the *in-vitro* measurements follow Combination I, Eqs. [37, 38].

Site and Soil

The site was located in a mixed deciduous-coniferous forest on a slope of Mt. Bantiger near Bern (Switzerland). The soil is classified as Luvisol according to FAO-UNESCO (1994) with a sandy-loam texture. The depths of separating the main horizons L-A-E-Bt-BC are at 0.02, 0.1, 0.4, and 0.7 m, respectively. Table 1 lists the pertinent physical properties.

Table 1: Pertinent soil properties

Soil depth m	Texture			Bulk density Mg m^{-3}	Porosity m^3 m^{-3}	K_{sat} m s^{-1}	p_H
	Sand $\%_w$	Silt $\%_w$	Clay $\%_w$				
0.15 - 0.25	54	35	11	1.35	0.49	1.8×10^{-6}	3.8
0.25 - 0.35	51	34	15	1.40	0.47	5.0×10^{-7}	4.0

In-situ Investigations

Experimental set-up

Figure 4 provides the scheme of instrumentation and sampling. Input q_S to the soil surface was through sprinkler irrigation. The sprinkler consisted of 100 metal tubes with inner diameters of 2 mm. They were mounted in a 0.1 m by 0.1 m square pattern through a square sheet metal of 1 m by 1m. A gear moved the suspended sheet metal 50 mm backward and forward in both horizontal dimensions such that it took approximately 1800 s for one tube outlet to sprinkle on the same spot. A battery-driven

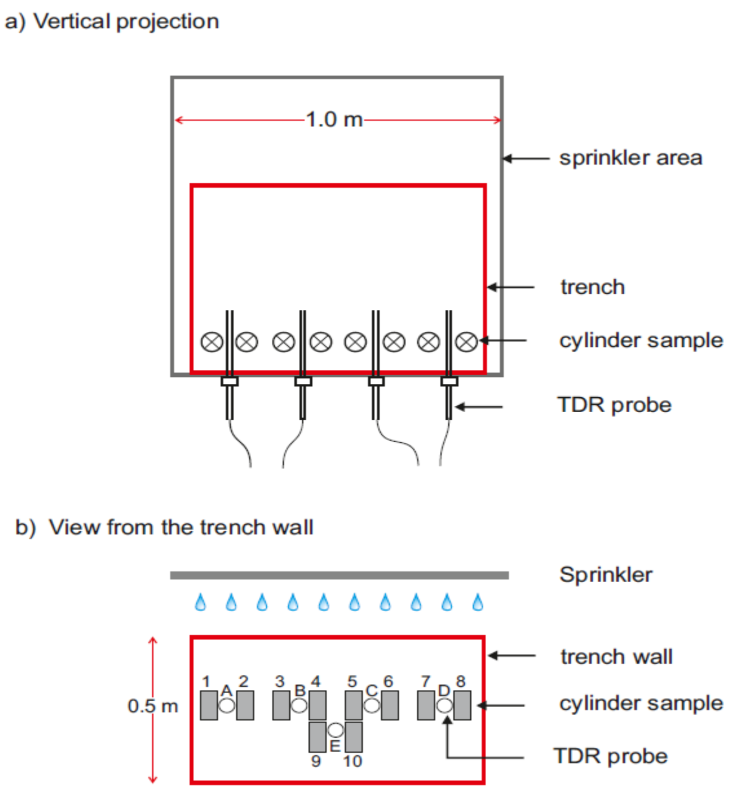

pump supplied water with preset rates from a tank through a manifold to the tubes.

Figure 4: Scheme of core sampling and TDR-instrumentation. A to E: Sites of TDR-waveguides; 1 to 10: Sites of core samples.

Time series of water contents $\theta_{dat}(Z_m,t)$were monitored with TDR-equipment. Each pair of wave guides consisted of two parallel stainless steel rods, 5 mm in diameter, 140 mm long and 30 mm apart. The rods were electrically connected via a 50 Ω coax cable with a SDMX50 50-Ω Coax Multiplexer, which was controlled by a CR 10X Campbell Micrologger. A Campbell TDR 100 device generated the electrical pulses and received the signals. TDR-measurements were recorded at 60-s intervals. Four paired TDR-probes were horizontally mounted at depths of Z_{m1} = 0.23 m in the soil profile 0.21 m apart and one probe at Z_{m2} = 0.33 m. The five TDR-sites are labeled from A to E, Fig. 4. Calibration was according to Roth et al. (1990).

Experiments and data

Three runs with sprinkler infiltration were performed in 2008 beginning on 28 June at 16:11 h, on 29 June at 16:23, and on 30 June at 16:48. During all three runs sprinkler irrigation lasted (T_E-T_B) = 3600 s, volume flux density was q_S = 1.4 x 10^{-5} m s^{-1} (50 mm h^{-1}), and the total volume applied amounted to Q_s = 50 mm. No ponding occurred. As an example, Fig. 5 depicts the time series $\theta_{dat}(Z_{m1},t)$ during $T_B \leq t \leq$ 50,000 s as monitored with the TDR-probe at site A during the three runs. Typically, $\theta_{dat}(Z_m,t)$ increases markedly from θ_{in} to θ_{max} shortly after T_B, followed by a period of approximately steady water content at θ_{max}, and a concave decline which asymptotically approaches the terminal water content θ_{end}. The indices in, max and end refer to the initial, maximum and final water contents of a $\theta_{dat}(Z_m,t)$-series.

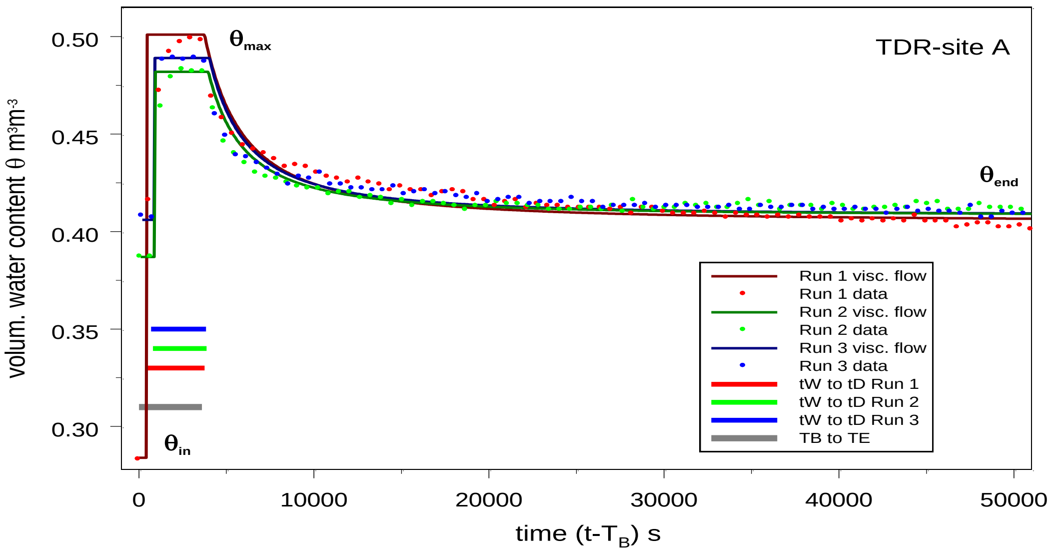

Figures 5: Time series of $\theta_{dat}(Z_{m1},t)$ due to sprinkler irrigation, Runs 1 to 3 at TDR-site A (dots; only any tenth data point is shown for clarity reasons.) The solid lines represent $\theta(Z_{m1},t)$-time series matched to the corresponding data $\theta_{dat}(Z_{m1},t)$. The horizontal bars depict the respective time lapses $t_W(Z_{m1}) \leq t \leq t_D(Z_{m1})$ and $T_B \leq t \leq T_E$.

Viscous-flow calibration

Viscous-flow calibration aims at deducing the parameters *F* and *L* from $\theta_{dat}(Z_m,t)$-series according to Eqs. [25-29] and Fig. 3. First, the depths Z_m of TDR-measurements have to be assessed with respect to Z_I. Because all fifteen time series show a distinct period of θ_{max} it is concluded that $0 \leq Z_m < Z_I$, Eq. [14]. Thus, the application of Eqs. [25-29] suffice for calibration. Second, the viscous-flow expressions are adapted as follows:

$$T_B \leq t \leq t_W(z): \qquad \theta(Z_m,t) = \theta_{in} \tag{48}$$

$$t_W(z) \leq t \leq t_D(z): \qquad \theta(Z_m,t) = \theta_{max} \tag{49}$$

$$t \geq t_D(z): \qquad \theta(Z_m,t) = (\theta_{max} - \theta_{end}) \cdot \left(\frac{t_D(Z_m) - T_E}{t - T_E} \right)^{1/2} + \theta_{end} \tag{50}$$

Whereas

$$t_D(Z_m) = T_E + \frac{t_W(Z_m) - T_B}{3} \tag{51}$$

A Mathcad-computer code (MathSoft, 2001) calculated Eqs. [48-51] and displayed the complete graph of each $\theta_{dat}(Z_m,t)$- and $\theta(Z_m,t)$-series during the period $T_B \leq t \leq$ 62,400 s. The four parameters $t_W(Z_m)$, θ_{in}, θ_{max}, and θ_{end} were optimized such that the entire graph best matched the data upon ocular inspection. Figure 5 also depicts the three time series of calibrated viscous-flow functions, $\theta(Z_m,t)$. Table 2 lists the results of viscous-flow matching, where the amplitude of the mobile water content is $w_A = (\theta_{max} - \theta_{end})$ (the index *A* refers to the amplitude of $\theta_{max} - \theta_{end}$.)

The wetting front velocity is $v = Z_m/t_W(Z_m)$, and F_{field} follows from Eq. [7], while the specific contact area is $L_{field} = w_A/F_{field}$ according to Eq. [6]. For the entire period $T_B \leq t \leq$ 62,400 s the volume flux density $q(Z_m,t)$ results from inserting $w(Z_m,t) = [\theta(Z_m,t) - \theta_{end}]$ into Eq. [9]. The total volume of flow $Q(Z_m)$ for the same period follows from inserting the parameters F_{field} and L_{field}, and the appropriate times into Eq. [35]. Table 3 lists the parameters F_{field}, L_{field}, the maximum volume flux density q_A related to w_A, and $Q(Z_m)$. The Reynolds numbers according to Eq. [12] are within $4.5 \times 10^{-3} < Re < 1.9 \times 10^{-2}$.

Thus, flow is laminar and viscous flow applies. The following compares the minima and maxima of F_{field}, L_{field}, and w_A, Tab. 3, with the corresponding frequency distributions of Hincapié and Germann (2009a) who analyzed with the viscous-flow approach 215 θ(z,t)-series from more than 20 soil profiles, wherer all θ(Z,t)-series were due to *in-situ* sprinkler irrigation. Film thicknesses in Tab. 3 in the range of $7.7 \leq F_{field} \leq 12.5$ µm is considered relatively thin because they score in the lower 10% of the frequency distribution. The specific contact areas $2350 \leq L_{field} \leq 8250$ m^2 m^{-3} are in the 40- to 60%-range of the distribution. The *w*-values in Tab.2 place within $0.021 \leq w_A \leq 0.096$ and cover the 20- to 90%-range of the cumulative frequency distribution of Hincapié and Germann (2009a).

Validation of the viscous flow approach

Goodness-of-fit between $\theta_{dat}(Z_m, t)$- and $\theta(Z_m,t)$-series is assessed with coefficients of determination r^2, once for the entire time range from T_B to (t_{end}-T_B) of 62,400 s, referred to as "all data" with r_{all}^2 and once excluding the section with the increasing branch of the time series, which is referred to as "plateau to tail", r_{pt}^2. The r^2-values from the third time frame using tail-data only i.e., from $t_D(Z)$ to t_{end} did not differ significantly from those of the second time frame.

Equation [29] approaches 0 asymptotically. It allows to estimate the drop of $w(Z_m,t)$ since the arrival of the draining front at $t_D(Z_m)$. Thus, under consideration of average $t_W(Z_m) - T_B = 772$ s from Tab. 2 and Eqs. [29, 51],

$$\frac{w(Z_m,t)}{w_S} = \left(\frac{t_D(Z_m) - T_E}{t - T_E}\right)^{1/2} \qquad [52]$$

yields on average a relative reduction of $w(Z_m,t_{end})$ to 4.4 x 10^{-3} of the mobile water content hitting Z_m at $t_D(Z_m)$, meaning that the interval from T_B to (t_{end}-T_B) of 62,400 s covered 99.5 % of the possible reduction. The procedure, Eq. [52], permits to estimate $w(Z_m, t_{end})$ at any pre-set t_{end}. However, the later t_{end} the more likely other processes may overwhelm viscous flow, like capillarity and evapo-transpiration.

Table 2: Results from matching the viscous-flow approach to the data: Arrival times $t_W(Z_m)$ of the wetting fronts at depth Z_m; volumetric water contents at the beginning, maximum and end, θ_{in}, θ_{max}, θ_{end}, mobile water content of the amplitude, w_A, and coefficients of determination of viscous-flow approach vs. data: r_{all}^2 refers to all data, while r_{pt}^2 includes only data belonging to the plateau and tail.

TDR-site	Run	$t_W(Z_m)$	θ_{in}	θ_{max}	θ_{end}	w_A	r_{all}^2	r_{pt}^2
		s	$m^3\ m^{-3}$	$m^3\ m^{-3}$	$m^3\ m^{-3}$	$m^3\ m^{-3}$	all data	plateau, tail
A	1	450	.284	.501	.405	.096	0.88	0.97
	2	800	.387	.482	.408	.074	0.91	0.98
	3	700	.406	.489	.408	.081	0.94	0.97
B	1	800	.382	.470	.442	.028	0.63	0.84
	2	1000	.435	.467	.446	.021	0.82	0.87
	3	800	.446	.470	.448	.022	0.75	0.81
C	1	500	.314	.478	.400	.078	0.68	0.97
	2	900	.389	.474	.406	.068	0.90	0.96
	3	660	.397	.481	.402	.079	0.91	0.98
D	1	750	.352	.510	.434	.076	0.23	0.93
	2	1100	.425	.511	.445	.066	0.81	0.93
	3	800	.442	.510	.446	.064	0.87	0.97
E	1	1620	.372	.462	.400	.062	0.66	0.97
	2	1700	.400	.450	.406	.044	0.92	0.97
	3	1620	.406	.455	.406	.048	0.95	0.97
av[1)]		772 [a)]	.389	.481	.420	.060		
SD[2)]		177 [a)]	.044	.019	.019	.022		
CV[3)]		0.23 [a)]	.112	.040	.046	.367		
CI[4)]		±117[a)]	± .028	± .012	± .013	± .014		

1) average from the 15 data of all the five sites and three runs

2) standard deviation

3) Coefficient of Variance: CV=SD/av

4) Confidence Interval with 5% error probability and 14 degrees of freedom

a) only the 12 $t_W(Z_m)$-values from sites A to D are included with 11 degrees of freedom

The averages of q_A and $Q(Z_m)$ serve as objective criteria for validation. They should not exceed the rate and volume of sprinkling i.e., $q_A \leq q_S$ and $Q(Z_m) \leq Q_S$. According to Tab. 3 average q_A = 1.9 x 10^{-5} m s^{-1} exceeds the sprinkler rate q_S = 1.4 x 10^{-5} m s^{-1} by 36%. However, expected q_S lies within the 95%-confidence interval of 1.23 x 10^{-5} $\leq q_A \leq$ 2.57 x 10^{-5} m s^{-1}. Likewise, Q_S = 50 mm lies within the 95%-confidence limits of 42 $\leq Q(Z_m) \leq$ 92 mm. Thus, the viscous-flow approach to infiltration seems valid from the statistical point of view. The simple experimental protocol hardly permits further analyses of the validity of the viscous-flow approach to infiltration. More detailed investigations are required to better separate the three kinds of partial viscous-flow variations, the spatial variation among the five TDR-sites, the uncertainties in applying viscous-flow, and uncertainties in the measurements.

Discussion

Viscous-flow theory assumes a discontinuous and steep increase of $\theta(Z_m,t)$ from θ_{in} to θ_{max}, whereas $\theta_{dat}(Z_m,t)$ show gradual increases which is ascribed to water sorption from the *WCW* to the stagnant parts of the permeable medium due to capillarity. The comparison $r_{all}^2 < r_{pt}^2$ indicates that capillarity is active during the early stage before the *WCW* is approaching the plateau. After that, viscous flow matches the data much better. Germann et al. (2007) empirically modeled the gradual increase with a series of ten superimposed *WCW*s which they termed rivulets. The superimposed rivulets added well up to the overall trailing wave during $t > t_D(Z)$.

Germann and al Hagrey (2008) applied the viscous-flow approach to $\theta(Z_m,t)$-series which were measured in the Kiel sand tank with TDR-probes at nine depths ranging from 0.2 to 1.8 m. The velocity of the wetting front remained constant during infiltration, therefore dF/dz = 0. Further, no trend with depth of the gradual increases of $\theta(Z_m,t)$ from θ_{in} to θ_{max} was discernible. Thus, Germann and al Hagrey (2008) concluded that the gradual increase is due to local processes most likely occurring within the control volume of the TDR-probes. Germann (2014) provides additional clues on the gradual increase of $\theta(Z_m,t)$.

Table 3: Results from viscous-flow interpretations: Film thickness F_{field}, specific contact area L_{field}, steady volume flux density q_A during $t_W(Z_m) \leq t \leq t_D(Z_m)$, comparison of q_A with q_S of 1.4 x 10^{-5} m s^{-1}, volume of flow $Q(Z_m)$ leaving depth Z_m during $t_W(Z_m) \leq t \leq$ 50,000 s, and comparison of $Q(Z_m)$ with Q_S of 50 mm.

TDR-site	Run	F_{field}	L_{field}	q_A x 10^{-6}	q_A/q_S	$Q(Z_m)$	$Q(Z_m)/Q_S$
		µm	m^2 m^{-3}	m s^{-1}	--	mm	--
A	1	12.5	7680	49	3.5	176	3.5
	2	9.4	7890	21	1.5	76	1.5
	3	10.0	8080	26	1.9	94	1.9
B	1	9.4	2990	8	0.6	29	0.6
	2	8.4	2500	5	0.4	17	0.3
	3	9.4	2350	6	0.4	22	0.5
C	1	11.8	6580	35	2.5	127	2.5
	2	8.8	7690	17	1.2	60	1.2
	3	10.3	7650	27	1.9	97	1.9
D	1	9.7	7850	23	1.6	83	1.7
	2	8.0	8250	13	0.9	49	1.0
	3	9.4	6830	18	1.3	65	1.3
E	1	7.9	7860	12	0.9	44	0.9
	2	7.7	5710	8	0.6	30	0.6
	3	7.9	6080	10	0.7	34	0.7
av[1)]		9.4	6400	19	1.4	67	1.34
SD[2)]		1.4	2000	12	0.9	44	0.87
CV[3)]		0.15	0.31	0.63	0.63	0.65	0.65
CI[4)]		± 0.8	± 1162	± 6.7	± 0.48	± 25	± 0.50

1) average from the 15 data of all the five sites and three runs

2) standard deviation

3) Coefficient of Variance: CV=SD/av

4) Confidence Interval with 5% error probability and 14 degrees of freedom

The difference (θ_{max} - θ_{in}) is the amplitude of the *WCW* arriving at Z_m. In the control volume occupied by the TDR probe the divergence $\Delta\theta$ = (θ_{in} – θ_{end}) is due to water abstraction from the *WCW* due to capillarity and subsequent storage during the passing of the *WCW* (probably the equilibrium part of capillary flow according to the Richards equation). $\Delta\theta$ reduces from the first to the third runs as the degree of saturation in the matrix increased. However, divergence is here not considered any further.

Table 4 summarizes the averages and SD of θ_{in}, θ_{max}, θ_{end}, and w_A from the three runs at each TDR-site. At each site the three water contents θ_{max} are much closer to one another than are the three θ_{in}. Yet no distinct sequences of θ_{max} are discernible from the first to the second and to the third runs among the five sites. The initial water contents vary the most, while the maximum and final water contents vary about the same value and considerably less than θ_{in}. Thus, the decrease of SD from θ_{in} to θ_{max} and θ_{end} suggests no strong impact of θ_{in} on θ_{max} and θ_{end}. However, the humid climate and preparatory experiments produced rather high θ_{in}-values, and no generalization should be drawn from the comparison.

Table 4: Viscous-flow matching: Averages and standard deviations SD of θ_{in}, θ_{max}, θ_{end}, and w_A of the three runs at each TDR-site A to E. Clearly, SD of θ_{in} exceed those of θ_{max} and θ_{end}.

TDR-Site	θ_{in}		θ_{max}		θ_{end}		w_A	
	$m^3\ m^{-3}$		$m^3\ m^{-3}$		$m^3\ m^{-3}$		$m^3\ m^{-3}$	
	av[1)]	SD[2)]	av	SD	av	SD	av	SD
A	.359	.0536	.491	.0078	.407	.0014	.084	.0092
B	.421	.0279	.469	.0014	.445	.0025	.024	.0031
C	.367	.0374	.478	.0029	.403	.0025	.075	.0050
D	.406	.0390	.510	.0005	.442	.0054	.068	.0052
E	.393	.0148	.455	.0050	.404	.0028	.051	.0077

1) average from the three runs at each TDR-site

2) standard deviation

Generally, the recessions of $\theta_{dat}(Z_m,t)$-series, Fig. 5, show concave bending during $t > t_D(Z_m)$ which follow rather closely the expected functions of Eq. [50]. Not shown here are the exceptional temporary convex bulges during $\theta_{dat}(Z_m,t)$-recession at TDR-sites B and D in all three runs. This is ascribed to temporary restrained viscous flow due to local water perching. The observations demonstrate sprinkling rates q_S being close to saturated flow q_{sat}, Eq. [42]. The condition was intentionally established for better comparison of the *in-situ* with the *in-vitro* investigations.

In-vitro investigations

The section provides the viscous-flow parameters from the core samples, Fig. 4, for comparison with those obtained from the field experiments.

Soil sampling and experimental set-up

Ten soil samples were collected in the profile according to Fig. 4, using beveled steel cylinders with inner and outer diameters of 76 and 80 mm, and heights of 100 mm. The samples were saturated in a bath by gradually increasing the water level. Metal sieves on either side of the cores kept the samples in the cylinders before their mounting between the top and bottom discs and hydraulically connecting them to the infiltration-drainage system, Fig. 6.

From the Darcy experiment, Eqs. [42, 44], follow K_{sat} and $q(p)$. The independent determination of $v(p)$, Eq. [45], requires the propagation of a tracer, for instance, of a temperature front forced on flow. Figure 6 depicts the design of the set-up. Input to the core is from two reservoirs. One contains water of ambient temperature T_0, the other one water of T= 48 °C. The stopcock allows switching of flow from one to the other reservoir. The overflow maintains atmospheric pressure of water input to the core sample. Two thermistors (Betathermistor 100K6A, Campbell Scientific Ltd., Logan Utah, US) measured temperature at Z_{m1} = 15 mm and Z_{m2} = 50 mm below the upper rim of the core mantle, and a 21X Micrologger (Campbell scientific Ltd.) recorded the measurements at 1-second intervals. The looked for velocity follows from $v(p) = (\Delta z)/[t_T(Z_{m2})-t_T(Z_{m1})]$, where $\Delta z = Z_{m2} - Z_{m1}$ and $t_T(Z_m)$ is the arrival time at Z_m of the first significant temperature increase.

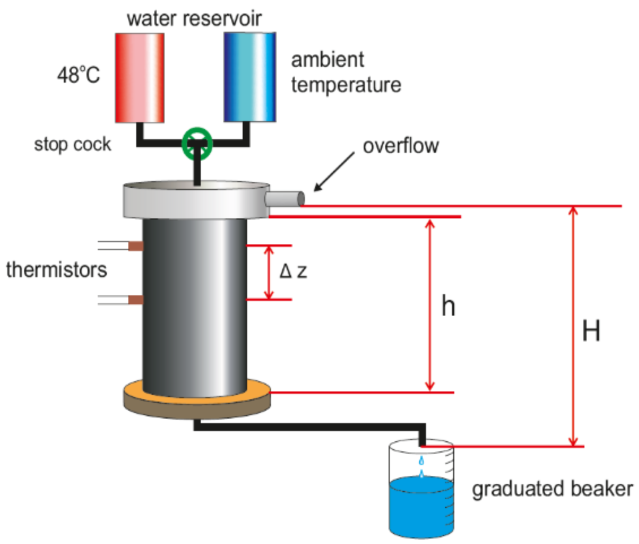

Figure 6: Experimental set-up. *H*: hydraulic head; *h*: height of sample; $\Delta z = Z_{m2}- Z_{m1}$; Z_{m1} and Z_{m2} are the thermistor depths at 15 and 50 mm below the upper rim of the soil core.

Experiments and data

Temperature increase was considered significant when the standard deviation of the previous 60 T-measurements exceeded 0.01°C, at which time the tracer front is thought to have arrived at Z_m. Temperature increase alters viscosity, however, only behind the temperature front. In principle, heat diffusion during Δt delays the arrival time of the heat front at Z_{m2}. This fact is in need of further investigations. Figure 7 illustrates $T(Z_{m1,2},t)$ and their standard deviations SD. The data are from sample 3, Run 2. Mishaps led to data missing from Run 2 of sample 1, Run 1 of sample 6, and from Runs 1 and 2 of sample 9. The hydraulic gradients were in the range of $2.25 \leq H/h \leq 2.38$.

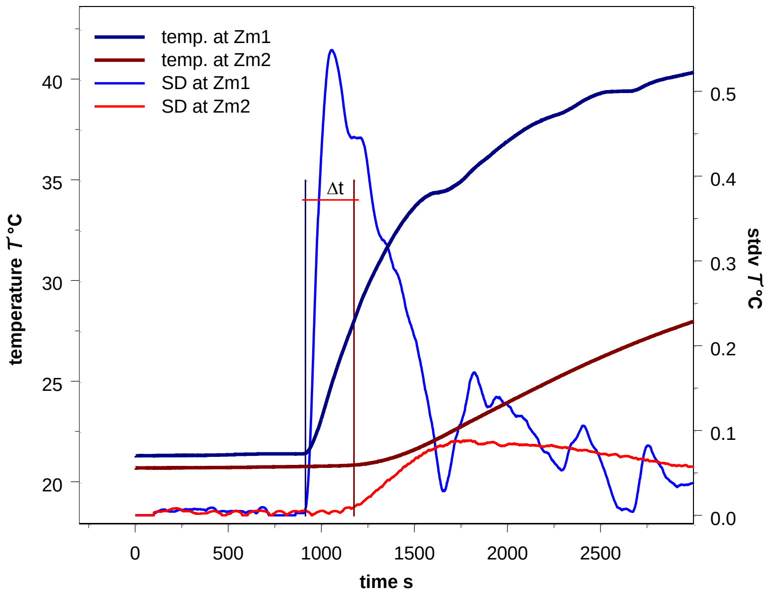

Figure 7

Figure 7: Time series of temperature $T(Z_m,t)$ and standard deviation SD of temperature's 60-s intervals at depths Z_{m1} = 15 mm and Z_{m2} = 50 mm below the rim of soil core 3, run 2. The vertical blue and red lines indicate the arrival times of the heat front, and Δt was used to estimate *v.*

Data interpretation

The experiments using the device in Fig. 6 deliver *q(p)* and *v(p).* According to Eqs. [42-45], they need to be divided by the hydraulic gradient $\Delta p/(\Delta z\ \rho\ g) = H/h$ in order to produce q_{sat} and v_{sat}. From Eq. [7] follows $w_{sat} = q(p)/v(p)$ and Eqs. [43, 42] lead to the parameters F_{sat} and L_{sat}. Table 5 compiles the results.

Discussion

During saturated flow the share of mobile water with respect to porosity amounts to $0.025 \leq w_{sat}/\varepsilon \leq 0.254$. The following compares the minima and maxima of F_{sat}, L_{sat}, and w_{sat}, Tab. 5, with the corresponding frequency distributions of Hincapié and Germann (2009a). Film thickness in Tab. 5 in the range of $3.7 \leq F_{sat} \leq 6.1$ µm is considered rather thin. The range of F_{sat} scores in the lowest 5% of the distribution. The specific contact areas, lying in the range of $3290 \leq L_{sat} \leq 32470$ m^2 m^{-3}, are in the

Table 5 : Film thickness F_{sat}, specific surface area L_{sat}, mobile water content w_{sat}, relative mobile water content w_{sat}/ε, and volume flux density q_{sat} from laboratory experiments.

Sample #	Run	F_{sat}	L_{sat}	w_{sat}	w_{sat}/ε	q_{sat} x 10^{-6}
		µm	m^2m^{-3}	m^3m^{-3}	---	m s^{-1}
1	1	4.4	7840	0.035	0.071	2.2
2	1	3.7	5960	0.022	0.042	1.0
	2	4.1	4820	0.020	0.039	1.1
3	1	3.7	3290	0.012	0.025	0.6
	2	4.2	7260	0.031	0.063	1.8
4	1	3.7	21570	0.081	0.165	3.7
	2	6.1	16770	0.103	0.207	12.5
5	1	4.6	20530	0.096	0.185	6.9
	2	4.3	15710	0.068	0.131	4.3
6	2	3.9	13350	0.053	0.106	2.8
7	1	4.6	17160	0.080	0.167	5.8
	2	4.2	15370	0.065	0.135	3.7
8	1	4.0	32470	0.132	0.254	7.1
	2	3.8	27650	0.107	0.206	5.3
10	1	3.7	6060	0.023	0.049	1.1
	2	3.8	7610	0.029	0.062	1.4
av[1)]		4.2	13960	0.061	0.121	3.8
SD[2)]		0.6	8030	0.036	0.068	3.1
CV[3)]		0.14	0.58	0.59	0.56	0.80

[1)] average from the 16 data of all the remaining 9 cores and suitable repetitions

[2)] standard deviation

[3)] Coefficient of Variance: CV=SD/av

90- to 100%-range, the mobile water contents place within $0.012 \leq w_{sat} \leq 0.132$ and cover a range from 20% to 98% within the cumulative frequency distribution. Typically, thin films of mobile water coupled with large specific contact areas feature fine textured soils but still allowing for viscous flow, however, the assessment contradicts the soil texture, Tab. 1.

The Reynolds numbers, Eq. [12], are within $5.0\times10^{-4} < Re < 2.2\times10^{-3}$. Thus, viscous flow is laminar and Darcy's (1856) law applies.

Comparison between *in-situ* and *in-vitro* applications of viscous flow

The comparison is based on graphical displays with groupings of w_{sat} vs. w_A, q_{sat} vs. q_A, F_{sat} vs. F_{field}, and L_{sat} vs. L_{field}. All the results from Cores 1 and 2 are assigned to all the results from TDR-site A, from Cores 3 and 4 to B, from Cores 5 and 6 to C, from Cores 7 and 8 to D, and from Core 10 to E. (See Fig. 4 for orientation.) The averages of the assigned data groups provide the anchor point of the corresponding distribution while the field-results are depicted along the horizontal axis and the lab-results along the vertical axis. These entirely qualitative topographical juxtapositions of the *in-situ* vs. the *in-vitro* results seem not suited for further statistical treatments.

The *w*-values from the two approaches, Fig. 8, are arranged around the 1:1 line, indicating $\langle w_A \rangle = \langle w_{sat} \rangle$. The wide spreads of w_{sat} assigned to TDR-sites B and D are mainly due to the variations among the cores 3 and 4, as well as among cores 7 and 8. Cautiously interpreted, the comparison supports the notion that the mobile water content can be deduced with either method, though keeping the sources of variation in mind.

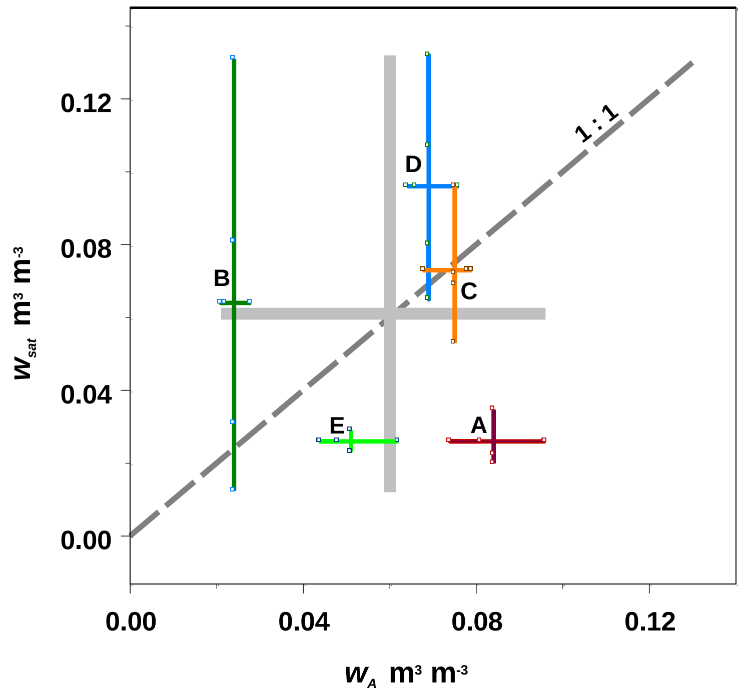

Figure 8

Figure 8: Comparison of mobile water contents *w* from *in-vitro* vs. *in-situ* experiments, w_{sat} vs. w_A. The symbols indicate individual measurements, the letters A to E refer to the TDR-wave guides and associated core samples, the grey cross covers the entire range of minimal and maximal mobile water contents, and the 1:1-line helps in the comparison.

The distributions of the volume flux densities, q_{sat} vs. q_A , from the two procedures, Fig. 9, are situated below the 1:1-line, revealing on the average (gray lines) an approximate ratio of q_{sat}/q_A = 1:5, and a similar ratio of their spreads.

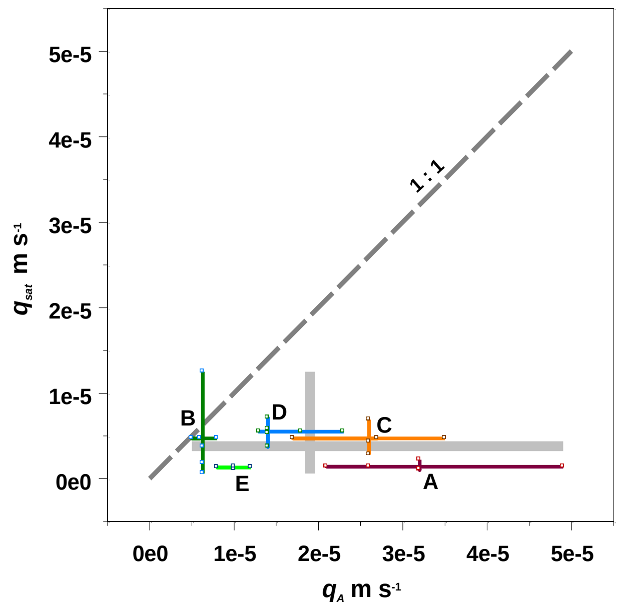

Figure 9

Figure 9: Comparison of volume flux densities from the *in-vitro* vs. *in-situ* experiments, q_{sat} , vs. q_A . (See Fig. 8 for further explanations.)

Most intriguing are the comparisons of *F* and *L*, Fig. 10, whose gray crosses are located on either side of, and distinctly away from the 1:1-line. The approximate ratios of the averages of L_{sat} / L_{field} = 2:1 and of F_{sat} / F_{field} = 1:4 hint at a methodological discrepancy between the two experimental procedures. Increasing *L*-values indicate increasing internal surface areas onto those momentum diffuses while increasing *F*-values are related with wider flow paths. Thus, some of the wider *in-situ* flow paths seem to have vanished in the core samples, and flow was apparently forced to narrower paths. However, the closeness of w_{sat} with w_A, Fig. 8, hardly permits such discrepancies in view of Eq. [6]. Also the apparent misinterpretation of texture with the same viscous-flow parameters indicates irregularities in their determination. Both, $w_A = (\theta_{\text{max}} - \theta_{\text{end}})$ and $w_{sat} = q_{sat}/v_{sat}$ emerge experimentally without direct reference to viscous flow while *F* and *L* evolve from it. The *WCW* due to sprinkler-irrigation is almost exclusively exposed to atmospheric pressure, Eq. [5, 7], whereas flow in the soil cores is driven by the pressure gradient, Eq. [44, 45]. Thus, the discrepancy between the two procedures is most likely related to ($\Delta p/\Delta z$) vs. (ρ g). Also the cause of the differences between q_{sat} vs. q_A point in the same direction.

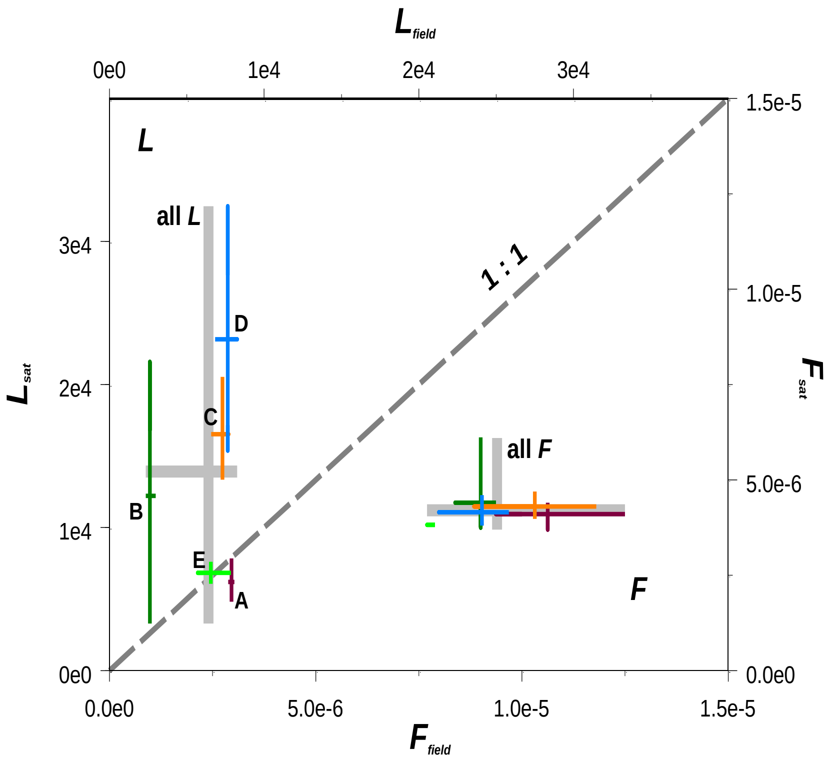

Figure 10

Figure 10: Comparison of specific contact lengths and the film thicknesses from the lab experiments, L_{lab} and F_{lab}, vs. those from the field experiments, L_{field} and F_{field}. The upper left triangle of the graph refers to L and the lower right one to F. (The symbols of the individual measurements are not shown for clarity reasons. See Fig. 8 for further explanations.)

Methodological improvements of the *in-vitro* procedures have to focus on the determination of the hydraulic gradient, for instance, by mounting manometers at the depths of the thermistors (i.e., performing Darcy's original experiment). Also scrutinizing the temperature-tracer procedure may help, however, the insensitivity of $F \propto v^{½}$ seems not the most efficient remedy. Methodological improvements of the field procedure have to focus on the mass balance i.e., on $Q(z)$ and q_A in comparison with Q_S and q_S, although the Confidence Intervals did not reveal statistically significant differences. Further, the observed gradual $\theta_{dat}(z,t)$-increases from θ_{in} to θ_{max} contrast with the corresponding discontinuous jumps expected from viscous flow as the comparison of Fig. 3 with Fig. 5 reveals. Thus, viscous flow may overestimate $Q(z)$ in that q_A is applied for too long a period of $t_W(z) \leq t \leq t_D(z)$. Germann et al. (2007) matched the observed gradual $\theta_{dat}(z,t)$-increases with a series of rivulets with delayed arrival times, each following viscous-flow rules. The rivulet procedure might provide the remedies for the overestimation of $Q(z)$ and q_A. However, the rivulet approach is considered of more a phenomenological approach rather than being strictly based on hydro-mechanical principles.

Summary and conclusions

The viscous flow approach to infiltration and drainage in permeable media is based on hydro-dynamic principles. The approach was applied to *in-situ* sprinkler infiltration into a soil close to saturation as well as to *in-vitro* flow in saturated soil cores collected from the same site. *In-vitro* tracing of flow velocities was with temperature shocks forced on the infiltrating water. The experiments produced the mobile water content *w* and the two parameters film thickness *F* and specific contact length *L*. Between the two kinds of experiments *F* and *L* differed by factors of 4 and 2, whereas *w*-values are considered equivalent, though within rather wide variations. It is therefore concluded that, with an improved protocol, *in-vitro* flow experiments may produce *F*- and *L*-parameters useful for modeling *in-situ* infiltration. The parameters are in the approximate ranges of $4 \leq F \leq 12$ µm and $2{,}300 \leq L \leq 35{,}000$ $m^2\ m^{-3}$. The widths of flow paths of 2*F* do not necessarily coincide with the popular perception of macropore dimensions. Likewise, the specific contact lengths in the km/m^2-range may call for reconsiderations of the ordinarily presumed preferential-flow geometries. Viscous flow along such fine structures is only possible if viscous and capillary forces simultaneously co-exist and compete whereby priority goes to viscous flow while water abstraction from the WCW is due to posterior action of capillarity.

The viscous-flow approach only requires that F and L are derived from the same cross-sectional area A and that the wetting fronts move freely. In particular, there is no requirement of a representative elementary volume, REV, in the sense of the Richards equation. These properties relax adherence to particular length- and time-restrictions beyond the event-based time and depth of front interception, T_I and Z_I. There are indications that viscous flow is rather tolerant on permeable-media lengths. The applicability of viscous flow to infiltration and drainage was demonstrated in numerous cases, ranging from the sub-mm- to the m-scale (see, for instance, Hincapié and Germann, 2009c; Germann and alHagrey, 2008). Moreover, Dubois (1991) reported approximate wetting front velocities of $v = 2 \times 10^{-4}$ m s^{-1} in cristalline rocks of the Mont Blanc massif in the three-corner region of France, Italy, and Switzerland. Dubois applied uranin- and eosin-tracers at a vertical distance of about 1800 m above the Mont Blanc car-tunnel which connects Chamonix in France with Courmayeur in Italy. He identified the tracers in seeps in the tunnel within 108 days after injection. Dubois' v-value scores at the lower 10% of the frequency distribution of 215 wetting front velocities reported by Hincapié and Germann (2009a). Water seeped into the tunnel at atmospheric pressure which indicates complete diffusion of momentum during flow, Eq. [2], while the v-value demonstrates similarity of flow with viscous flow in soils.

Water abstraction from the *WCW* is the result of the co-existents of capillarity and viscosity. Mdaghri et al. (1997), for instance, ran similar *in-situ* infiltrations into a poorly structured clay loam in July at a site near Bratislava (Slovakia) at low θ_{in}. There, it took two consecutive sprinkler experiments applying 27 mm of water each time before getting a $\theta_{dat}(Z_m,t)$-series at the 0.3-m depth which looked similar to those in Fig. 5. In contrast, Vadilonga et al. (2008) reported unimpeded viscous flow in well-structured clay-loams also at low θ_{in}. Thus, θ_{in} may impact θ_{max} and θ_{end}, however, functional voids in the minimum range of F of about 10 µm also need to be considered.

For hydrological interpretations sprinkler experiments are frequently run with infiltration rates q_S simulating heavy rain storms. But rain-fall infiltrations into the Coshocton lysimeters have demonstrated that intensities as low as 10 mm d^{-1} suffice to initiate rapid flow reaching the 2.4-m depth (Germann, 1986).

A better confirmed relationship $q_S \propto v^{3/2}$, Eq. [47], for broader ranges of permeable media and q_S would greatly advance the viscous-flow approach. Despite the supporting evidence Shiozowa and Fujimaki (2004) and Hincapié and Germann (2009b) have provided, still many more investigations are required to properly assess the validity of the macropore-flow restriction. But if it would apply than the *F*- and *L*-parameters determined in saturated soil cores could be used to scale with Eq. [47] a broad range of input rates, ideally covering $0 \leq q_S \leq K_{sat}$ of a particular permeable medium. Then, modeling sequences of variable $P(q_S,T_B,T_E)$-pulses can be based on kinematic wave theory according to Lighthill and Witham (1955). To that purpose, Germann (2014) has demonstrated the complete congruence of viscous flow according to Stokes (1845) and Lamb (1932) with the kinematic wave theory of Lighthill and Whitham (1955), whereby only fixing to 3 of the exponent in Eq. [9] was required. Thus, the *in-vitro* determination of *F* and *L*, the subsequent scaling of *F* according to Eq. [47] to any input rate in the range of $0 < q_S < K_{sat}$, and routing a broad range of input pulses *P* with the kinematic-wave theory would greatly advance the applicability of the approach to infiltration and drainage. For instance, quick assessments of advancing wetting- and related pollutant-fronts to fragile unconfined aquifers would become feasible. Germann and Levy (1986) and Germann (2014) reported fast front advancements to unconfined groundwater tables, though without their further evaluation. In addition, *L* also expresses the vertical specific contact area per unit volume of the medium onto which momentum diffuses. This area is considered relevant for any other exchanges like heat, ions, particles, and water between the stagnant and the mobile parts of a permeable medium during preferential flow.

However, the viscous-flow approach is based on hydro-mechanical principles similar to Darcy's law. Although no REV is required, the approach averages flow properties and is thus not suited for deducing the flow parameters *F* and *L* directly from micro images of presumed flow structures in permeable media.

In conclusion, viscous flow as presented here is considered an adequate response to the call of Alberti and Cey (2011) that "*New models for representing unsaturated flow in macro-porous systems are needed along with carefully measured data sets for model testing*."

Acknowledgment

Boris Faybishenko encouraged submission of the paper to the Vadose Zone Journal's Special Section on Soil as Complex Systems. The positive assessments of two anonymous reviewers greatly helped to stream-line the manuscript.

References

Alberti, D.R., and E.E. Cey. 2011. Evaluation of macropore flow and transport using three-dimensional simulation of tension infiltration experiments. Vadose Zone J. 10:603-617; doi: 10.2136/vzj2010.0104.

Coppola, A., H.H. Gerke, A. Comegna, A. Basile, and V. Comegna. 2012. Dual-permeability model for flow in shrinking soil with dominant horizontal deformation. Water Resour. Res. 48, W08527; doi: 10.1029/2011WR011376.

Darcy, H. 1856. Les fontaines publiques de la ville de Dijon. Dalmont, Paris.

Dubois, J.-D. 1991. Typologie des aquifers du cristallin : Exemples des massifs des Aiguilles Rouges et du Mont-Blanc. Ph.D.-dissertation 950. Department of Civil Engineering, EPFL, Lausanne (Switzerland), unpublished.

FAO-UNESCO. 1994. *Soil Map of the World*. ISRIC, Wageningen (NL).

Flammer, I., A. Blum, A. Leiser, and P. Germann. 2001. Acoustic assessment of flow patterns in unsaturated soil. *J. of Applied Geophys*. 46**:**115-128.

Germann, P.F. 1986. Rapid drainage response to precipitation. J. Hydrol. Proc. 1: 3-13.

Germann, P.F. 2014. *Preferential Flow – Stokes Approach to Infiltration and Drainage*. Geographica Bernensia, Bern (Switzerland), 199 p.

Germann, P.F., and S. A. al Hagrey. 2008. Gravity-driven and viscosity-dominated infiltration in a full-scale sand model. Vadose Zone J. 7: 1160-1169. doi: 10.2136/vzj2007.0172.

Germann, P., and B. Levy. 1986. Rapid response of shallow ground water tables upon infiltration – A call for information. EOS 2/25/86: 92.

Germann, P., A. Helbling, and T. Vadilonga. 2007. Rivulet approach to rates of preferential infiltration. Vadose Zone J. 6: 207-220. Doi: 10.2136/vzj2006.0115

Hincapié, I., and P. Germann. 2009a. Abstraction from infiltrating water content waves during weak viscous flows. Vadose Zone J. 8:996–1003; doi:10.2136/vzj2009.0012

Hincapié, I., and P. Germann. 2009b. Impact of initial and boundary conditions on preferential flow. J. Contaminant Hydrol 104:67-73.

Hincapié, I., and P. Germann. 2009c. Gravity-driven viscous flow in sand boxes assessed with neutron radiography. Vadose Zone J. 8:891-901; doi:10.2136/vzj2009.003.

Jarvis, N. 2007. Review of non-equilibrium water flow and solute transport in soil macropores: Principles, controlling factors, and consequences for water quality. Eur. J. Soil Sci. 58:523-546; doi: 10.1111/j.1365-2389.2007.00915.x

Karlen, M. 2008. Vergleich zwischen im Labor und im Feld gemessenen mobilen Wassergehalten. M.Sc.-Thesis, Faculty of Science, University of Bern, 108 p. (unpublished)

Lamb, H. 1932. *Hydrodynamics.* Sixth Edition. Cambridge University Press (UK).

Lazouskaya, V., Y. Jin, and D. Or. 2006. Interfacial interactions and colloid retention under steady flows in a capillary channel. J. Colloid. Interf. Sci. 303:171-184.

Lighthill M.J., and G.B. Witham. 1955. On kinematic waves, I. Flood movement in long rivers. Proc. R. Soc. London, Ser. A, 229: 281-316.

Lin, S.P., and C.Y. Wang. 1986. Modeling wavy film flows. p. 931–951. *In:* Encyclopedia of Fluid Mechanics, Vol. 1. Gulf Publishing Co., Houston, TX.

MathSoft. 2001. *Manual Mathcad 2000 Professional.* MathSoft, Inc. Cambridge, MA (USA).

Maxwell, J.C.1866. On the Dynamical Theory of Gases. Phil. Trans. clxxvii. 49.

Mdaghri Alaoui, A., P. Germann, L. Lichner, and V. Novak. 1997. Preferential transport of water and ^{131}Iodide in a clay loam assessed with TDR-techniques and boundary-layer flow theory. Hydrology and Earth System Sciences 4:813-822.

Newton, I. 1729. *The Mathematical Principles of Natural Philosophy – Translation into English*. Vol. II, p. 184, Benjamin Motte, London (UK).

Richards, L.A. 1931. Capillary conduction of liquids through porous mediums. Physics 1: 318.333.

Roth, K., R. Schulin, H. Flühler, and W. Attinger. 1990. Calibration of Time Domain Reflectometry. Water Resour. Res. 26(10):2267-2273.

Shiozawa, S., and H. Fujimaki. 2004. Unexpected water content profiles and flux limited one-dimensional downward infiltration in initially dry granular media. Water Resour. Res. 40:W07404, doi: 10.1029/2003WR002197.

Stokes, G.G. 1845. On the theories of internal friction of fluids in motion. Transactions of the Cambridge Philosophical Society 8, pp. 287–319.

Vadilonga, T., X. Ubeda, P.F. Germann, and M. Lorca. 2008. Effects of prescribed burning on soil hydrological parameters. Hydrol. Proc. 22:4249-4256.